

The structural, mechanical, electronic, optical and thermodynamic properties of $t\text{-X}_3\text{As}_4$ ($X = \text{Si}, \text{Ge}$ and Sn) by first-principles calculations

R. Yang¹, Y. Ma¹, Q. Wei¹, D. Zhang², Y. Zhou³

¹ School of Physics and Optoelectronic Engineering, Xidian University, Xi'an, Shaanxi 710071, PR China

² National Supercomputing Center in Shenzhen, Shenzhen 518055, PR China

³ Leihua Electronic and Technology Research Institute, Aviation Industry Corporation of China, Wuxi, Jiangsu 214063, PR China

Received July 3, 2018, in final form October 19, 2018

The structural, mechanical, electronic, optical and thermodynamic properties of the $t\text{-X}_3\text{As}_4$ ($X = \text{Si}, \text{Ge}$ and Sn) with tetragonal structure have been investigated by first principles calculations. Our calculated results show that these compounds are mechanically and dynamically stable. By the study of elastic anisotropy, it is found that the anisotropic of the $t\text{-Sn}_3\text{As}_4$ is stronger than that of $t\text{-Si}_3\text{As}_4$ and $t\text{-Ge}_3\text{As}_4$. The band structures and density of states show that the $t\text{-X}_3\text{As}_4$ (Si, Ge and Sn) are semiconductors with narrow band gaps. Based on the analyses of electron density difference, in $t\text{-X}_3\text{As}_4$ As atoms get electrons, X atoms lose electrons. The calculated static dielectric constants, $\epsilon_1(0)$, are 15.5, 20.0 and 15.1 eV for $t\text{-X}_3\text{As}_4$ ($X = \text{Si}, \text{Ge}$ and Sn), respectively. The Dulong-Petit limit of $t\text{-X}_3\text{As}_4$ is about $10 \text{ J mol}^{-1} \text{ K}^{-1}$. The thermodynamic stability successively decreases from $t\text{-Si}_3\text{As}_4$ to $t\text{-Ge}_3\text{As}_4$ to $t\text{-Sn}_3\text{As}_4$.

Key words: $t\text{-X}_3\text{As}_4$, mechanical properties, optoelectronic properties, thermodynamic properties, first-principles calculations

PACS: 61.82.Bg, 62.20.dc, 71.20.Be, 71.15.Mb

1. Introduction

Liu and Cohen predict the $\beta\text{-C}_3\text{N}_4$ possesses the property of low compressibility. The structural and electronic properties of IV_3V_4 compounds have attracted more and more attention [1]. The hardness of the cubic silicon nitride was experimentally determined to be 35.31 GPa as the third hardest material after diamond and cubic boron nitride [2]. The thermal stability of the cubic silicon nitride was studied by X-ray powder diffraction and scanning electron microscopy which shows that the material is stable up to 1673 K in air. So, the material is suitable for engineering superhard ceramics for high temperature structural applications [2]. IV_3V_4 compounds have important potential applications in technical and scientific fields. The group IV nitrides have low compressibility and high hardness [3]. They have a wide application prospect in cutting [3]. Ching predicts the properties of the group IV nitrides using first principles theory [1]. Feng investigates the properties of pseudocubic- X_3P_4 ($X = \text{C}, \text{Si}, \text{Ge}$ and Sn) by using the first principle calculations [1]. They find that the modulus decreases with the atom change from C to Sn [1].

The structural and electronic properties of pseudocubic- X_3As_4 are investigated by using first principles method [1]. The pseudocubic- C_3As_4 is predicted to be metallic, pseudocubic- Si_3As_4 , Ge_3As_4 and Sn_3As_4 are semiconductors [4]. Although X_3As_4 have a wide range of applications in physics and chemistry, little research has been conducted regarding its mechanical and optical properties. Due to the lack of relevant experimental data at present, if we want to understand the application of tetragonal X_3As_4 , further theoretical and computational research on its properties should be done.

In this work, the structural parameters, mechanical, electronic, optical and thermodynamic properties of the tetragonal X_3As_4 are calculated by using the first-principles method based on plane waves and pseudo-potentials. By consulting the literature, we find that nobody has ever conducted experimental studies of the properties of the X_3As_4 ($X = Si, Ge$ and Sn). Therefore, we do not have the experimental data to compare with.

2. Computational methods

The structural optimization, mechanical, electronic, optical and thermodynamic properties of $t-X_3As_4$ are calculated by using the density functional theory (DFT) with the generalized gradient approximation (GGA) parameterized by Perdew, Burke and Ernzerhof (PBE) in the CASTEP code [5]. The band structures, electronic density of states (DOS) are calculated by PBE0 hybrid functional. The phonon spectra and phonon density of states (PHDOS) are calculated by using first-principles linear response method. Plane wave cut-off energy is set at 610 eV. The convergence test and energy cut-off analysis of k -point mesh samples show that the convergence of the Brillouin zone sampling and the kinetic energy cut-off are reliable and satisfy the computational requirements [6, 7]. The Broyden-Fletcher-Goldfarb-Shanno (BFGS) minimization scheme is used in geometry optimization. The value of self-consistent field tolerance threshold is set as 5.0×10^{-6} eV/atom. The maximum Hellmann-Feynman force, the maximum stress and the maximum displacement are set to be 0.01 eV/Å, 0.02 GPa and 5.0×10^{-4} Å in geometry optimization, respectively. The Monkhorst-Pack k -points in the first irreducible Brillouin zone are given as $10 \times 10 \times 13$ for $t-X_3As_4$, respectively. The mechanical, electronic, optical and thermodynamic properties of $t-X_3As_4$ are computed according to the optimized crystal structures and parameters.

3. Results and discussions

3.1. Structural properties

The $t-X_3As_4$ has a tetragonal structure with I-42M (No. 121). Figure 1 shows the crystal structures of $t-X_3As_4$ at 0 GPa. The $t-Si_3As_4$, $t-Ge_3As_4$ and $t-Sn_3As_4$ are all centro-symmetry structures (0, 0, 0) with 14 atoms/unit cell. The lattice parameters and volumes of $t-X_3As_4$ at 0 GPa are calculated on the basis of geometry optimization and are presented in table 1. The density values of $t-X_3As_4$ are 4.15015 g/cm³, 5.19889 g/cm³ and 5.46287 g/cm³, respectively.

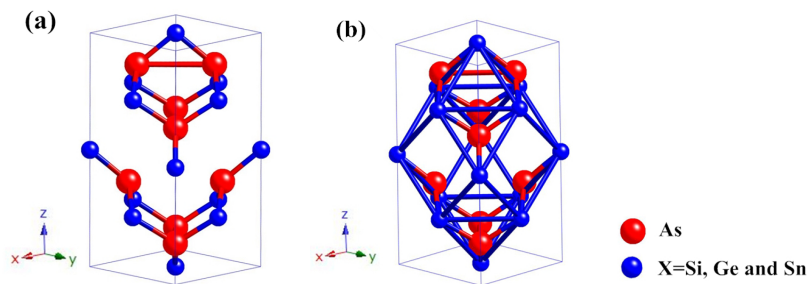


Figure 1. (Colour online) Crystal structures of $t-Si_3As_4$, $t-Ge_3As_4$ and $t-Sn_3As_4$ (I-42M, No. 121).

Table 1. Lattice constants a , b , c (Å) and volume (Å³) of the $t-X_3As_4$.

Structure	a	b	c	α	β	γ	V
Si_3As_4	5.36	5.36	10.69	90.00	90.00	90.00	307.24
Ge_3As_4	5.48	5.48	11.00	90.00	90.00	90.00	330.56
Sn_3As_4	5.83	5.83	11.73	90.00	90.00	90.00	398.66

3.2. Mechanical properties

The nine independent quantities of the elastic constants for t-X₃As₄ are calculated and presented in table 2. The mechanical stabilities of t-X₃As₄ can be estimated by elastic constants. In this work, the mechanical stabilities and mechanical moduli of t-X₃As₄ are approximated by the corresponding relationships for a tetragonal crystal class [8–11]. The elastic stability criteria of tetragonal phases are given as follows [12]:

$$\begin{aligned} C_{11} > 0, \quad C_{33} > 0, \quad C_{44} > 0, \quad C_{66} > 0, \\ (C_{11} - C_{12}) > 0, \quad (C_{11} + C_{33} - 2C_{13}) > 0, \\ 2(C_{11} + C_{12}) + C_{33} + 4C_{13} > 0. \end{aligned} \quad (1)$$

As indicated in table 2, the calculated elastic constants of the t-X₃As₄ do satisfy the criteria, indicating that they are mechanically stable. The t-Si₃As₄ exhibits the largest elastic constants of C_{11} , C_{22} , C_{33} . For the t-Si₃As₄ and the t-Sn₃As₄, the calculated C_{11} and C_{22} are equal and they are larger than C_{33} . Hence, the mechanical strength in [100] and [010] directions is stronger than that in [001] direction. Moreover, C_{44} , C_{55} and C_{66} denote the shear moduli in (100), (010) and (001) crystal planes, respectively. For t-Ge₃As₄, the values of C_{11} and C_{22} are the same and smaller than C_{33} . Hence, the mechanical strength in [100] and [010] directions are smaller than that in [001] direction. From table 2, the C_{44} , C_{55} of t-X₃As₄ are equal and they are larger than C_{66} . Therefore, the shear moduli at (100) and (010) crystal planes are larger than that of (001) crystal planes.

From the calculated elastic constants, other mechanical parameters such as bulk modulus (B), shear modulus (G), Young's modulus (E) and Poisson's ratio (ν) can be derived using Voigt-Reuss-Hill (VRH) approximation [8]. For t-X₃As₄, based on elastic constants, the Reuss shear modulus (G_R) and the Voigt shear modulus (G_V) are as follows:

$$G_R = 15/[4(S_{11} + S_{22} + S_{33}) - 4(S_{12} + S_{13} + S_{23}) + 3(S_{44} + S_{55} + S_{66})], \quad (2)$$

$$G_V = (C_{11} + C_{22} + C_{33} - C_{12} - C_{13} - C_{23})/15 + (C_{44} + C_{55} + C_{66})/5. \quad (3)$$

The Reuss bulk modulus (B_R) and the Voigt bulk modulus (B_V) are defined as

$$B_R = 1/[(S_{11} + S_{22} + S_{33}) + 2(S_{12} + S_{13} + S_{23})], \quad (4)$$

$$B_V = (C_{11} + C_{22} + C_{33})/9 + 2(C_{12} + C_{13} + C_{23})/9, \quad (5)$$

where the relationship between S_{ij} and C_{ij} is shown as

$$[S_{ij}] = [C_{ij}]^{-1}. \quad (6)$$

In the above formulae, the C_{ij} represents the elastic stiffness matrix and the S_{ij} represents the elastic flexibility matrix. The Hill's averages are taken from the averages of the two [8]

$$B = (B_V + B_R)/2, \quad (7)$$

$$G = (G_V + G_R)/2. \quad (8)$$

The Young's modulus, E , and Poisson's ratio, ν , can be calculated by the equations

$$E = 9BG/(3B + G), \quad (9)$$

Table 2. Calculated independent elastic constants of the t-X₃As₄ (X = Si, Ge and Sn).

Species	C_{11}	C_{12}	C_{13}	C_{22}	C_{23}	C_{33}	C_{44}	C_{55}	C_{66}
Si ₃ As ₄	97.34	35.86	36.85	97.34	36.85	94.60	49.34	49.34	42.90
Ge ₃ As ₄	80.97	30.70	34.87	80.97	34.87	85.04	39.06	39.06	32.60
Sn ₃ As ₄	54.68	24.29	27.06	54.68	27.06	52.30	25.16	25.16	21.49

Table 3. Calculated mechanical moduli of t-X₃As₄, including bulk modulus (B_V , B_R and B), shear modulus (G_V , G_R and G), Young's modulus (E) and Poisson's ratio (ν), B/G and H_V , in GPa.

Species	B_V	B_R	G_V	G_R	B	G	E	ν	B/G
Si ₃ As ₄	56.49	56.48	40.30	38.27	56.49	39.28	95.67	0.22	1.44
Ge ₃ As ₄	49.76	49.66	31.91	30.50	49.71	31.20	77.42	0.24	1.59
Sn ₃ As ₄	35.38	35.38	19.91	18.42	35.38	19.16	48.70	0.27	1.85

$$\nu = (3B - 2G)/[2(3B + G)]. \quad (10)$$

From (4) to (10), the calculated physical quantities are presented in the table 3.

From the calculated results, t-Si₃As₄ has the largest value of bulk modulus among t-X₃As₄, which indicates that t-Si₃As₄ has a lower compressibility. The shear modulus of t-Si₃As₄ is the largest in t-X₃As₄, indicating that t-Si₃As₄ has a strong rigidity. The Young's modulus values of t-X₃As₄ show that t-Si₃As₄ has a larger hardness.

The Poisson's ratio represents the stability of the shear strain of the crystal. For a typical metal, the value should be 0.33. For the ionic-covalent crystal, the value ranges from 0.2 to 0.3. Poisson's ratio of the strong covalent crystal is relatively small, usually below 0.15 [8]. For t-X₃As₄, the Poisson's ratios show that they are ionic-covalent crystal.

The ratio B/G reflects the brittleness or ductility of a material, and the critical value is close to 1.75 [13]. Below 1.75, the material shows brittleness; otherwise it shows toughness. As indicated in table 3, the B/G values for t-Si₃As₄ and t-Ge₃As₄ are smaller than 1.75, and the B/G value for t-Sn₃As₄ is higher than 1.75. Hence, t-Si₃As₄ and t-Ge₃As₄ show brittleness and t-Sn₃As₄ shows toughness.

It is well known that elastic anisotropy plays an important role in engineering science and crystal physics. The shear anisotropic factor for the (100) shear planes between [011] and [010] directions can be written by [14]:

$$A_1 = 4C_{44}/(C_{11} + C_{33} - 2C_{13}). \quad (11)$$

For the (010) shear plane between [101] and [001] direction is:

$$A_2 = 4C_{55}/(C_{22} + C_{33} - 2C_{23}). \quad (12)$$

For the (001) shear planes between [110] and [010] direction is:

$$A_3 = 4C_{66}/(C_{11} + C_{22} - 2C_{12}). \quad (13)$$

For isotropic crystal, the factors A_1 , A_2 and A_3 must be 1, while the deviation from 1 is a measure of the degree of the elastic anisotropy. Furthermore, since the compound is tetragonal, rather than cubic, the shear anisotropic factors are not sufficient to describe the elastic anisotropy. Therefore, the anisotropy of the linear bulk modulus should be considered. The anisotropy of the bulk modulus along a and c axes relative to the anisotropy along b axis can be estimated using the following equations:

$$A_{Ba} = B_a/B_b, \quad A_{Bc} = B_c/B_b. \quad (14)$$

When the value is 1, it represents an elastic isotropy, but if it is not equal to 1, it is an elastic anisotropy. Where B_a , B_b and B_c are the bulk moduli along different crystal axes, defined as

$$B_a = a(dP/da) = \Lambda/(1 + \alpha + \beta), \quad (15)$$

$$B_b = b(dP/db) = B_a/\alpha, \quad (16)$$

$$B_c = c(dP/dc) = B_a/\beta, \quad (17)$$

$$\Lambda = C_{11} + 2C_{12}\alpha + C_{22}\alpha^2 + 2C_{13}\beta + C_{33}\beta^2 + 2C_{23}\alpha\beta, \quad (18)$$

Table 4. The shear anisotropic factors A_1, A_2, A_3 , compressibility anisotropy factors A_{Ba}, A_{Bc} , percentage anisotropy in compressibility A_B and shear A_G , bulk modulus along the tetragonal crystallographic axes a, b, c (B_a, B_b and B_c , in GPa) in tetragonal I-42M(121) space group.

	A_1	A_2	A_3	A_{Ba}	A_{Bc}	A_B	A_G	B_a	B_b	B_c
Si ₃ As ₄	1.67	1.67	1.40	1.00	1.00	0.00	0.03	171.17	171.17	166.12
Ge ₃ As ₄	1.62	1.62	1.30	1.00	1.20	0.00	0.03	140.82	140.82	168.47
Sn ₃ As ₄	1.90	1.90	1.41	1.00	1.02	0.00	0.04	105.62	105.62	107.23

$$\alpha = \frac{(C_{11} - C_{12})(C_{33} - C_{13}) - (C_{23} - C_{13})(C_{11} - C_{13})}{(C_{33} - C_{13})(C_{22} - C_{12}) - (C_{13} - C_{23})(C_{12} - C_{23})}, \quad (19)$$

$$\beta = \frac{(C_{22} - C_{12})(C_{11} - C_{13}) - (C_{11} - C_{12})(C_{23} - C_{12})}{(C_{22} - C_{12})(C_{33} - C_{13}) - (C_{12} - C_{23})(C_{13} - C_{23})}. \quad (20)$$

In addition, the percentage of elastic anisotropy for bulk modulus A_B and shear modulus A_G in polycrystalline materials can be used as follows:

$$A_B = (B_V - B_R)/(B_V + B_R), \quad (21)$$

$$A_G = (G_V - G_R)/(G_V + G_R). \quad (22)$$

The implication of the definition is that the value of zero corresponds to elastic isotropy and the value of 100% identifies the largest elastic anisotropy.

The calculated results are listed in table 4. It is seen that t-X₃As₄ are elastic anisotropic. The t-Sn₃As₄ shows to be more anisotropic than t-Si₃As₄ and t-Ge₃As₄. For t-X₃As₄, the bulk moduli along a axis are equal to that along the b . For t-Si₃As₄, the bulk modulus along c axis is smaller than that along a axis and b axis. For t-Ge₃As₄ and t-Sn₃As₄, the bulk moduli along c axis are larger than that along a axis and b axis. In addition, we also noticed that the percentage bulk moduli anisotropy A_B is smaller than shear modulus anisotropy A_G , suggesting that the structures are anisotropic in compressibility.

3.3. Phonon spectra

The calculated phonon dispersion spectra of t-X₃As₄ at 0 GPa are shown in figure 2. No any imaginary phonon frequencies in the entire Brillouin zone confirms that t-X₃As₄ are dynamically stable [15, 16]. Since there are seven atoms in the protocell of t-X₃As₄, the crystal should have twenty one dispersion relationships in theory. That is, there should be twenty one phonon spectra calculation curves, which shows that the calculated results in this paper are consistent with the theoretical conclusions. Some of the twenty one phonon spectral curves overlap in some range of wave vectors. There are three acoustic branches and eighteen optical branches. Lattice vibrational modes play a major role in Raman scattering and infrared absorption at point Γ . From figure 2 (a) and figure 3 (a), we can see that an optical gap exists in the phonon dispersion spectrum of t-Si₃As₄. This is due to the large quality difference between Si atom and As atom. From figure 2 (b) and figure 3 (b), we can observe that the optical band gap of t-Ge₃As₄ is smaller than that of t-Si₃As₄, which is due to the mass difference between Ge and As being smaller. A similar situation occurs in t-Sn₃As₄.

The phonon density of states (PHDOS) of t-X₃As₄ is calculated by CASTEP and shown in figure 3, respectively. For t-Si₃As₄, we can observe that in the range of 0.8–6.8 eV, the total PHDOS is mainly from As, which indicates that the vibration of As atoms is dominant in this frequency band. In the range of 9.5–13.0 eV, the total PHDOS is mainly from Si, which indicates that the vibration of Si atoms is dominant in this frequency band. For t-Ge₃As₄, in the range of 0.2–6.1 eV, the total PHDOS is mainly from As, which indicates that the vibration of As is dominant in this frequency band. In the range of 6.2–8.8 eV, the total PHDOS is from Ge and As, which shows that Ge and As have a similar vibrational probability. For t-Sn₃As₄, in the range of 0.2–4.0 eV, the total PHDOS is from Sn and As, which shows that Sn and As have a similar vibrational probability. And in the range of 4.2–7.6 eV, the total PHDOS is mainly from As and partial from Sn, which indicates that the vibration of As is dominant in this frequency band.

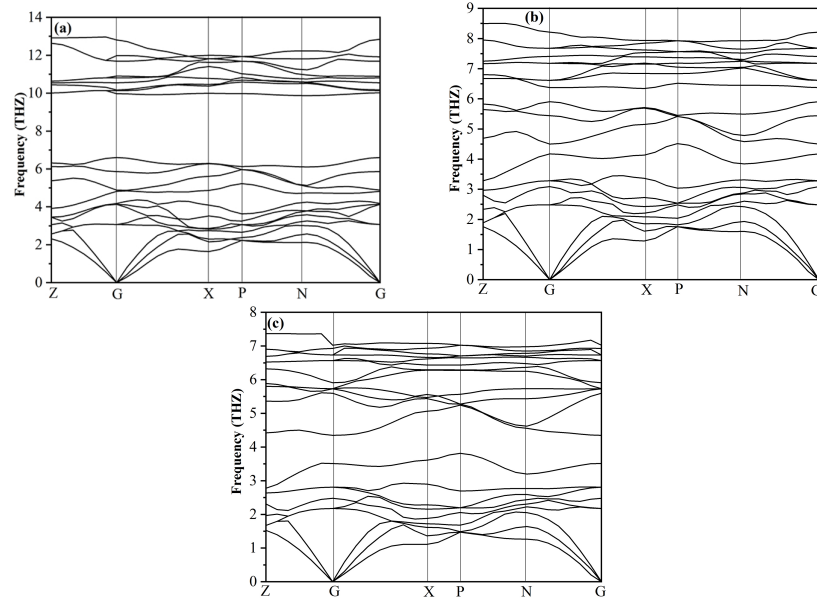


Figure 2. The phonon band structures (a) t-Si₃As₄, (b) t-Ge₃As₄, (c) t-Sn₃As₄.

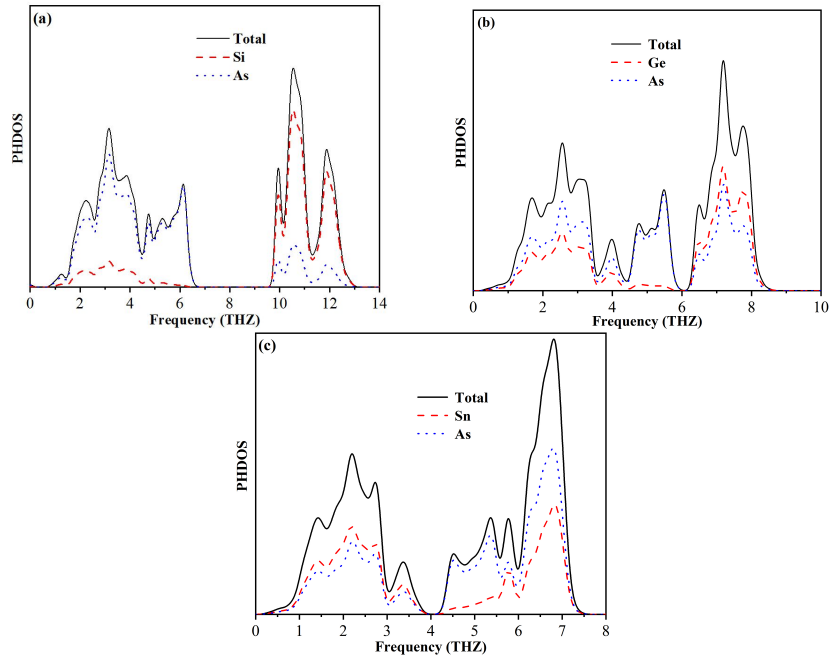


Figure 3. (Colour online) The phonon density of states (PHDOS) (a) t-Si₃As₄, (b) t-Ge₃As₄ and (c) t-Sn₃As₄.

3.4. Band structures and densities of states

The electronic properties of t-X₃As₄ are analyzed at 0 GPa. The DOS is calculated to have a further insight into the bonding characteristics of t-X₃As₄.

As indicated in figure 4, for t-Si₃As₄, the valence maximum is at high symmetric Γ -point and the conduction band minimum is at Z-point, which indicates that t-Si₃As₄ is an indirect band semiconductor with a band gap of 1.438 eV. For t-Ge₃As₄, the valence maximum is at high symmetric Γ -point and the

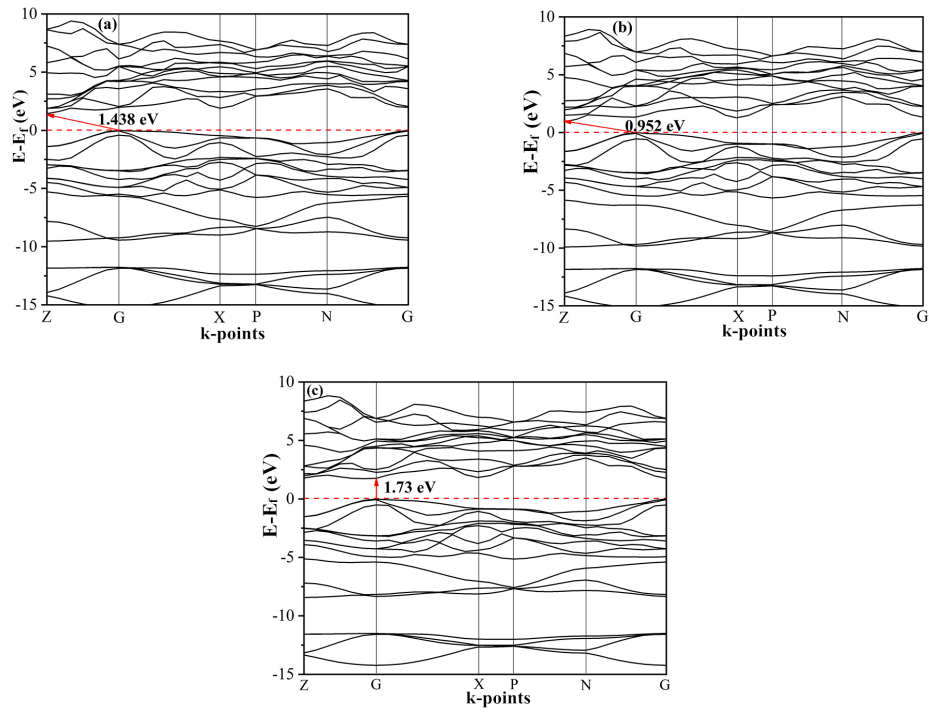


Figure 4. (Colour online) The band structures (a) $t\text{-Si}_3\text{As}_4$, (b) $t\text{-Ge}_3\text{As}_4$, (c) $t\text{-Sn}_3\text{As}_4$.

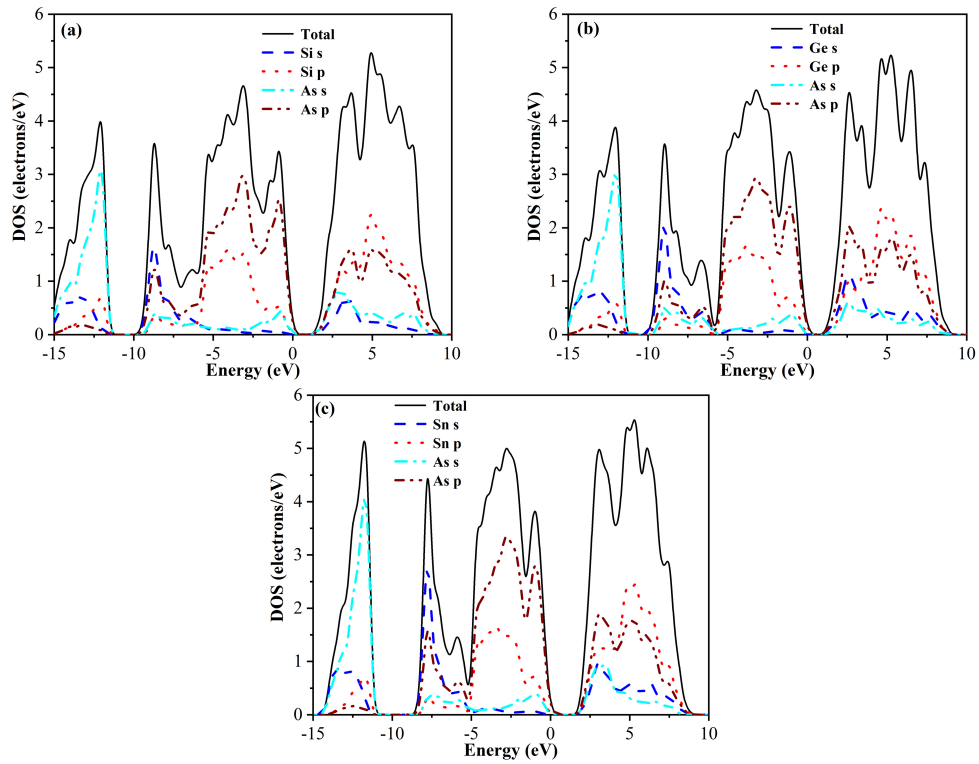


Figure 5. (Colour online) The electronic densities of states (a) $t\text{-Si}_3\text{As}_4$, (b) $t\text{-Ge}_3\text{As}_4$, (c) $t\text{-Sn}_3\text{As}_4$.

conduction band minimum is at Z-point, which indicates that t-Ge₃As₄ is an indirect band semiconductor with a band gap of 0.952 eV. For t-Sn₃As₄, the highest point of the valence band and the lowest point of the conduction band are at the Γ point. It shows that t-Sn₃As₄ is a direct band semiconductor with a band gap of 1.73 eV.

The density of states of t-X₃As₄ are presented in figure 5. For t-Si₃As₄, the main bonding peaks are in the range of -15–10 eV. The total DOS in the valence band mainly comes from As *s* and As *p*, with partially from Si *s* and Si *p*. Si *p* and As *p* contribute most to the total DOS in the conduction band, with partially from As *s* and Si *s*. For t-Ge₃As₄, the total DOS in the valence band mainly comes from As *s*, As *p* and Ge *s*, with partially from Ge *p*. In the conduction band, the total DOS mainly come from Ge *p* and As *p* with partially from Ge *s* and As *s*. For t-Sn₃As₄, the total DOS in the valence band mainly comes from As *s*, As *p* and Sn *s*, with partially from Sn *p*. In the conduction band, the total DOS mainly come from Sn *p* and As *p* with partially from Sn *s* and As *s*.

3.5. Electron density difference and Mulliken charge population

In order to investigate the chemical bonding, the electron density differences are calculated and the results are shown in figure 6. The electron density differences are the discrepancy between the electron densities of the total system and the unperturbed electron densities of X (Si, Ge and Sn) and As [16]. The contour plots show the electron density differences (between -0.2 and 0.2) due to the formation of chemical bonds in the I-42M lattice, which are relative to the electron density in an isolated atom. It is helpful to analyze how chemical bonds are formed. The electron density differences are useful for identifying the types of chemical bonds. From figure 6, we can see that As atoms get electrons, X (Si, Ge and Sn) lose electrons. The electrovalent bond is formed between X (Si, Ge and Sn) atoms and As atoms. The combination of X and As atoms is dependent on the ionic effect of Coulomb attraction. In order to further investigate the bonding behaviour of the three materials, we also obtain the Mulliken charge population. The Mulliken population results are given in table 5. Table 5 gives a quantitative determination of the number of loss electrons per X (Si, Ge and Sn) atom, the number of acquired electrons per X (Si, Ge and Sn) and the charger of per X atom and per As atom after the formation of Si₃As₄. From table 5, it is shown that the bonding behaviour of t-X₃As₄ is a combination of covalent and ionic nature.

3.6. Optical properties

Dielectric function is the most common characteristic of materials. It can characterize the response of materials to incident electromagnetic waves [17]. Optical properties of materials can usually be evaluated on the basis of a complex dielectric function, which depends on the frequency. Complex dielectric function is shown as follows [18]:

$$\varepsilon(\omega) = \varepsilon_1(\omega) + i\varepsilon_2(\omega), \quad (23)$$

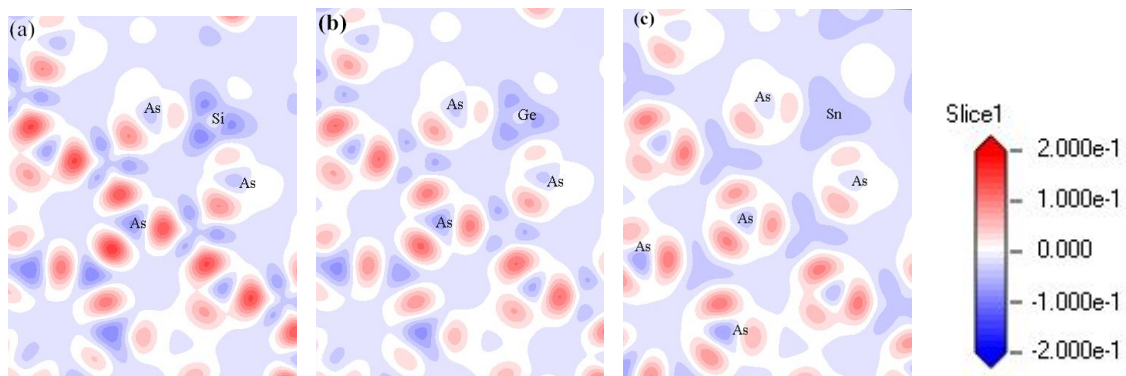


Figure 6. (Colour online) Electron density difference distribution for (a) t-Si₃As₄, (b) t-Ge₃As₄, (c) t-Sn₃As₄.

Table 5. The calculated atomic Mulliken charges (e) for t-X₃As₄ (X = Si, Ge and Sn).

Structure	Species	<i>s</i>	<i>p</i>	Total	Charge (e)
Si ₃ As ₄	Si(1)	1.42	2.42	3.83	0.17
	Si(2)	1.43	2.39	3.82	0.18
	Si(3)	1.43	2.39	3.82	0.18
	As(1)	1.63	3.50	5.13	−0.13
	As(2)	1.63	3.50	5.13	−0.13
	As(3)	1.63	3.50	5.13	−0.13
	As(4)	1.63	3.50	5.13	−0.13
Ge ₃ As ₄	Ge(1)	1.56	2.39	3.95	0.05
	Ge(2)	1.56	2.37	3.93	0.07
	Ge(3)	1.56	2.37	3.93	0.07
	As(1)	1.67	3.38	5.04	−0.04
	As(2)	1.67	3.38	5.04	−0.04
	As(3)	1.67	3.38	5.04	−0.04
	As(4)	1.67	3.38	5.04	−0.04
Sn ₃ As ₄	Sn(1)	1.55	2.28	3.82	0.18
	Sn(2)	1.53	2.26	3.79	0.21
	Sn(3)	1.53	2.26	3.79	0.21
	As(1)	1.60	3.55	5.15	−0.15
	As(2)	1.60	3.55	5.15	−0.15
	As(3)	1.60	3.55	5.15	−0.15
	As(4)	1.60	3.55	5.15	−0.15

where $\varepsilon_1(\omega)$ is the real part, $\varepsilon_2(\omega)$ is the imaginary part. The real and imaginary parts of the dielectric function are given in figure 7 (a). The calculated static dielectric constants, $\varepsilon_1(0)$, are 15.5, 20.0 and 15.1 eV for t-Si₃As₄, t-Ge₃As₄ and t-Sn₃As₄, respectively. For t-Si₃As₄, t-Ge₃As₄ and t-Sn₃As₄, the real parts of dielectric function enhance with an increasing photon energy and get to the highest values at about 1.94, 1.30 and 1.48 eV, respectively. The imaginary part curves increase with an increase of photon energy and get to the highest values at about 3.69, 3.54 and 3.97 eV.

Refractive index $n(\omega)$ and extinction coefficient $k(\omega)$ of t-X₃As₄ can be obtained from $\varepsilon_1(\omega)$ and $\varepsilon_2(\omega)$:

$$n(\omega) = \left\{ \frac{1}{2} \left[\varepsilon_1(\omega) + \sqrt{\varepsilon_1^2(\omega) + \varepsilon_2^2(\omega)} \right] \right\}^{1/2}, \quad (24)$$

$$k(\varepsilon) = \left\{ \frac{1}{2} \left[-\varepsilon_1(\omega) + \sqrt{\varepsilon_1^2(\omega) + \varepsilon_2^2(\omega)} \right] \right\}^{1/2}. \quad (25)$$

The static refractive indices are found to be 3.94, 4.48 and 3.89 eV for t-Si₃As₄, t-Ge₃As₄ and t-Sn₃As₄, respectively. The values of $n(\omega)$ increase with an increasing photon energy in the visible light region, and in the ultraviolet band, reach the peaks at about 2.24, 1.40 and 1.67 eV for t-Si₃As₄, t-Ge₃As₄ and t-Sn₃As₄, respectively. In figure 7 (c), the reflective coefficients are displayed. The main peaks lie at 11.1, 6.55 and 10.8 eV, respectively.

Vibrational Raman spectroscopy is one of the widely used optical techniques in materials science. It is a standard method for quality control of a production line. It is very effective in determining the occurrence of new phases or structural changes at extreme conditions. Moreover, it can be used in the absence of a long-range structural order as for liquid or amorphous materials. Raman spectroscopy can link Raman lines to specific microstructures. In order to further verify the crystal structure, the micro-Raman spectra of t-Si₃As₄, t-Ge₃As₄ and t-Sn₃As₄ were calculated by first-principles. Our Raman intensity results excited by the 514.5 nm incident light are presented in figure 7 (d). The Raman line

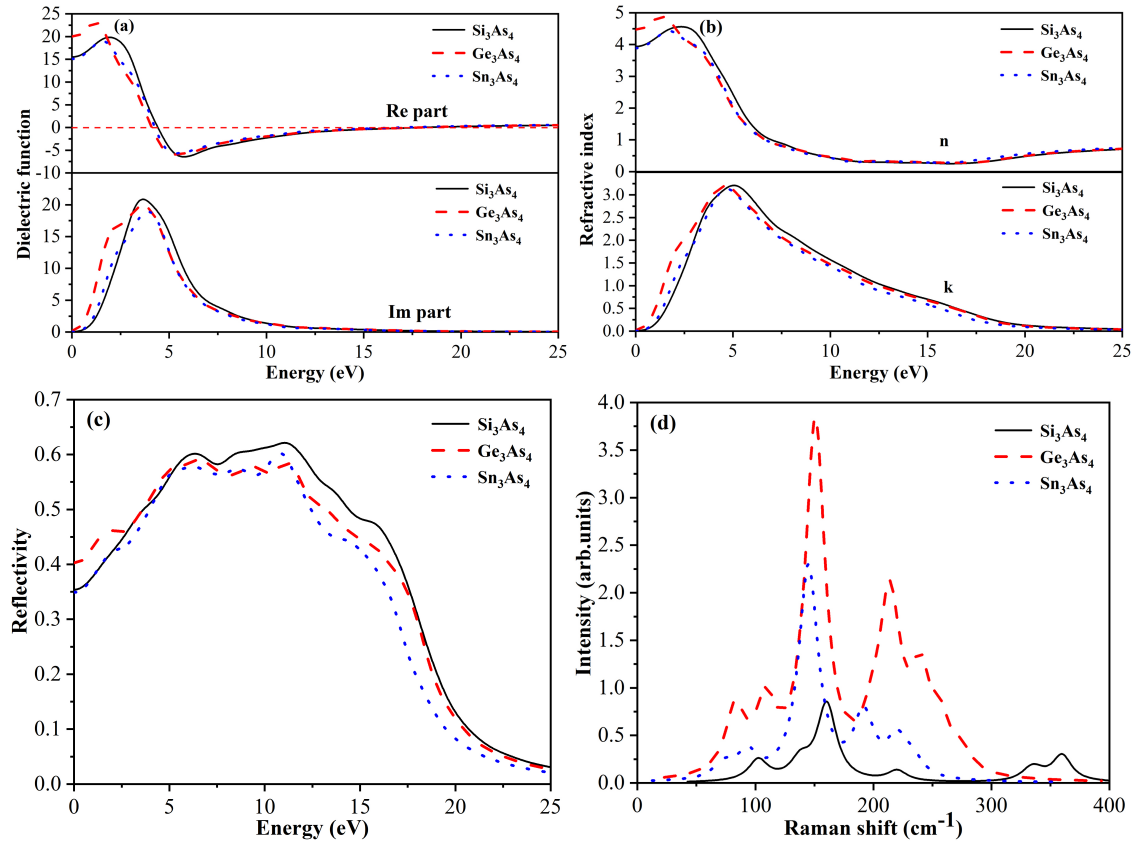


Figure 7. (Colour online) (a) Real and imaginary parts of dielectric function, (b) real and imaginary parts of refractive index, (c) optical reflectivity spectrum, (d) Raman intensities for the $t\text{-X}_3\text{As}_4$ (X = Si, Ge and Sn).

shape is assumed to be Lorentzian, and the line-width is fixed at 10 cm^{-1} FWHM. The peaks mainly locate at 103, 161, 220, 336, and 361 cm^{-1} for $t\text{-Si}_3\text{As}_4$, 83.8, 109, 151, 214 and 239 cm^{-1} for $t\text{-Ge}_3\text{As}_4$, 92.8, 145, 191 and 219 cm^{-1} for $t\text{-Sn}_3\text{As}_4$.

3.7. Thermodynamic properties

For $t\text{-X}_3\text{As}_4$, we have studied the thermodynamic properties based on the phonon density of states at 0–1000 K temperature. According to CASTEP, the heat capacity is contributed by the lattice, C_V is

$$C_V(t) = k \int \frac{\left(\frac{\hbar\omega}{kT}\right)^2 \exp\left(\frac{\hbar\omega}{kT}\right)}{\left[\exp\left(\frac{\hbar\omega}{kT}\right) - 1\right]^2} F(\omega) d\omega. \quad (26)$$

Debye temperature can be used to measure the properties of crystals, such as melting temperature, elastic constants and specific heat [19]. With the development of cryogenic technology, the deviation between Debye theory and practice increases. It is shown that the Debye temperature is different at different temperatures. According to the temperature dependence of Debye temperature at a constant volume, some general theoretical predictions can be made [20]. Heat capacity in Debye model is given by

$$C_V^D(T) = 9Nk \left(\frac{T}{\theta_D}\right)^3 \int_0^{\theta_D/T} \frac{x^4 e^x}{(e^x - 1)^2} dx, \quad (27)$$

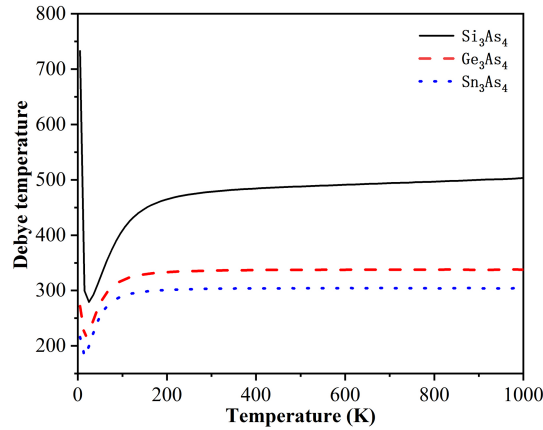


Figure 8. (Colour online) The relationship between Debye temperature and temperature for $t\text{-X}_3\text{As}_4$.

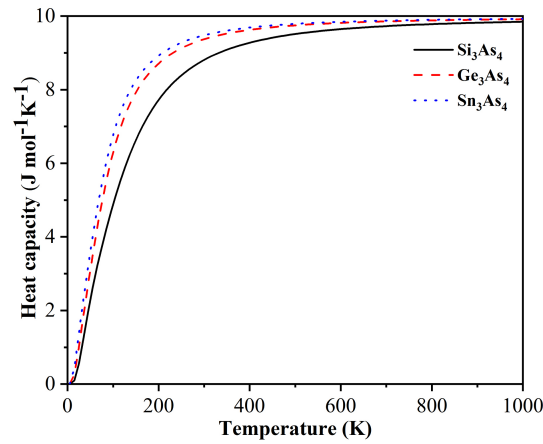


Figure 9. (Colour online) The relationship between the constant volume heat capacity and temperature for $t\text{-X}_3\text{As}_4$.

where N is the number of atoms per cell. Thus, the value of the Debye temperature, θ_D , at a certain temperature, T , is obtained by calculating the actual heat capacity according to equation (24), then by inverting equation (25). The relations of the Debye temperature with temperature are given as figure 8. The Debye temperature of $t\text{-Si}_3\text{As}_4$ is larger than that of $t\text{-Ge}_3\text{As}_4$ and $t\text{-Sn}_3\text{As}_4$ between 0 and 1000 K. It is found that the Debye temperature decreases with an increase of temperature, and then increases after reaching a minimum, and that minimum values are 279, 216 and 181 K for $t\text{-Si}_3\text{As}_4$, $t\text{-Ge}_3\text{As}_4$ and $t\text{-Sn}_3\text{As}_4$. While above 300 K, θ_D of $t\text{-Si}_3\text{As}_4$, $t\text{-Ge}_3\text{As}_4$ and $t\text{-Sn}_3\text{As}_4$ show weak temperature dependence and approach the constant values. At 1000 K, values of θ_D are 503 K, 338 K and 304 K, respectively.

Heat capacity is an important parameter in condensed matter physics. It can also describe the vibrational properties in the heat transition process. The lattice (or phonon) contribution and the electron contribution are two main sources of heat capacity. The former contributes most at a low temperature, while the latter plays an important role at a high temperature. The relations of the constant volume heat capacity C_V with temperature are presented in figure 9 for $t\text{-X}_3\text{As}_4$. It can be seen that these heat capacities increase rapidly with the temperature increase at a lower temperature. At a high temperature, heat capacities rise slowly and are close to the Dulong-Petit limit. It indicates that the atomic interactions in $t\text{-X}_3\text{As}_4$ occur at a low temperature. The Dulong-Petit limit of $t\text{-X}_3\text{As}_4$ is about $10 \text{ J mol}^{-1} \text{ K}^{-1}$. The variations of the entropy, enthalpy and free energy with temperature at 0 GPa are shown in figure 10. All values are given in the form of per $t\text{-X}_3\text{As}_4$ formula unit. It is noted that the free energy decreases with the temperature increase, and the entropy increases more rapidly than that of enthalpy as temperature

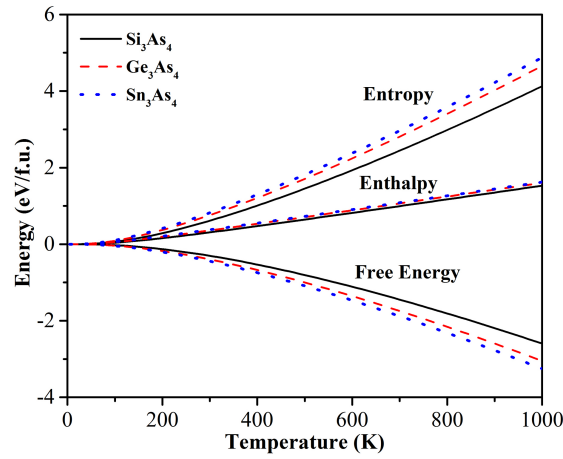


Figure 10. (Colour online) The entropy, the enthalpy and the free energy of $t\text{-X}_3\text{As}_4$ as a function of temperature.

Table 6. The entropy, enthalpy and free energy (eV/f.u.) for $t\text{-X}_3\text{As}_4$.

	Si_3As_4	Ge_3As_4	Sn_3As_4
Entropy	0.602	0.744	0.807
Enthalpy	0.305	0.355	0.377
Free energy	-0.298	-0.388	-0.436

increases. The calculated values of the entropy, enthalpy and free energy of $t\text{-X}_3\text{As}_4$ at room temperature are listed in table 6. All absolute values of the entropy, enthalpy and free energy for $t\text{-Sn}_3\text{As}_4$ are larger than those of $t\text{-Si}_3\text{As}_4$ and $t\text{-Ge}_3\text{As}_4$ under the temperature range from 0 to 1000 K, which means that $t\text{-Sn}_3\text{As}_4$ are less stable than $t\text{-Si}_3\text{As}_4$ and $t\text{-Ge}_3\text{As}_4$. From the figure 10 and table 6, we can see that the descending order of thermodynamic stability is from $t\text{-Si}_3\text{As}_4$ to $t\text{-Ge}_3\text{As}_4$ to $t\text{-Sn}_3\text{As}_4$.

4. Conclusion

For the novel predicted $t\text{-X}_3\text{As}_4$, the structural, mechanical, electronic, optical and thermodynamic properties are studied by the first-principles calculations. It is found that $t\text{-X}_3\text{As}_4$ are stable by elastic constants and phonons analysis. The $t\text{-Sn}_3\text{As}_4$ shows to me more anisotropic than $t\text{-Si}_3\text{As}_4$ and $t\text{-Ge}_3\text{As}_4$. Due to a larger mass difference between As and Si atom, there is a larger optical band gap in the dispersion curves of $t\text{-Si}_3\text{As}_4$. By analyzing the density of phonon states in $t\text{-Si}_3\text{As}_4$, $t\text{-Ge}_3\text{As}_4$ and $t\text{-Sn}_3\text{As}_4$, we can see that the vibration of As atoms is dominant in the frequency range of 0.8–6.8 eV, 0.2–6.1 eV and 4.2–7.6 eV, respectively. The vibration of Si and Ge atoms is dominant in the band of 9.5–13 eV and 6.2–8.8 eV, respectively. For $t\text{-Sn}_3\text{As}_4$, in the range of 0.2–4.0 eV, the total PHDOS is from Sn and As, which shows that Sn and As have the similar vibrational probability. The band structures and densities of state show that the $t\text{-X}_3\text{As}_4$ ($X = \text{Si}$ and Ge) are indirect band gap semiconductors with narrow band gaps of 1.438 and 0.952, respectively. The band structure of $t\text{-Sn}_3\text{As}_4$ shows that it is a direct band gap semiconductor. By the analysis of electron density difference and Mulliken charge population, it is found that X (Si, Ge and Sn) atoms lose electrons, and As atoms acquire electrons. The static refractive indices are found to be 3.94, 4.48 and 3.89 eV for $t\text{-Si}_3\text{As}_4$, $t\text{-Ge}_3\text{As}_4$ and $t\text{-Sn}_3\text{As}_4$, respectively. The $\epsilon_1(0)$ are 15.5, 20.0 and 15.1 eV for $t\text{-Si}_3\text{As}_4$, $t\text{-Ge}_3\text{As}_4$ and $t\text{-Sn}_3\text{As}_4$, respectively. The Debye temperature of $t\text{-Si}_3\text{As}_4$ is larger than that of $t\text{-Ge}_3\text{As}_4$ and $t\text{-Sn}_3\text{As}_4$. The Dulong-Petit limit of $t\text{-X}_3\text{As}_4$ is about $10 \text{ J mol}^{-1} \text{ K}^{-1}$. The thermodynamic stability of $t\text{-Si}_3\text{As}_4$ is higher.

5. Acknowledgements

This work is supported by the Natural Science Basic Research plan in Shanxi Province of China [No. 2016JM1026] and supported by the 111 Project [B17035]. This work is also supported by Leihua Electronic and Technology Research Institute, Aviation Industry Corporation of China (No. MJZ-2016-S-44).

References

1. Hu J., Huang S., Xie Z., Hu H., Cheng W., *J. Phys.: Condens. Matter*, 2007, **19**, No. 49, 496215, doi:10.1088/0953-8984/19/49/496215.
2. Jiang J.Z., Kragh F., Frost D.J., Ståhl K., Lindelov H., *J. Phys.: Condens. Matter*, 2001, **13**, No. 22, L515–L520, doi:10.1088/0953-8984/13/22/L11.
3. Liu A.Y., Cohen M.L., *Phys. Rev. B*, 1990, **41**, No. 15, 10727–10734, doi:10.1103/PhysRevB.41.10727.
4. Hu C., Feng Y.P., *Phys. Rev. B*, 2006, **74**, No. 10, 104102, doi:10.1103/PhysRevB.74.104102.
5. Yang R., Ma S., Wei Q., Du Z., *Z. Naturforsch., A: Phys. Sci.*, 2017, **72**, No. 9, 805–810, doi:10.1515/zna-2017-0155.
6. Zhang X.D., Shi H.F., *Mater. Sci. Technol.*, 2014, **30**, No. 6, 732–738, doi:10.1179/1743284713Y.0000000423.
7. Yang R., Zhu C., Wei Q., Du Z., *J. Phys. Chem. Solids*, 2016, **98**, 10–19, doi:10.1016/j.jpcs.2016.05.012.
8. Ding Y., *Physica B*, 2012, **407**, No. 12, 2190–2200, doi:10.1016/j.physb.2012.02.040.
9. Perdew J.P., Burke K., Ernzerhof M., *Phys. Rev. Lett.*, 1996, **77**, No. 18, 3865–3868, doi:10.1103/PhysRevLett.77.3865.
10. Wu Z.-J., Zhao E.-J., Xiang H.-P., Hao X.-F., Liu X.-J., Meng J., *Phys. Rev. B*, 2007, **76**, No. 5, 054115, doi:10.1103/PhysRevB.76.054115.
11. Xiao B., Feng J., Zhou C.T., Jiang Y.H., Zhou R., *J. Appl. Phys.*, 2011, **109**, No. 2, 023507, doi:10.1063/1.3532038.
12. Feng J., Xiao B., Zhou R., Pan W., Clarke D.R., *Acta Mater.*, 2012, **60**, No. 8, 3380–3392, doi:10.1016/j.actamat.2012.03.004.
13. Pugh S.F., *Lond. Edinb. Dubl. Philos. Mag.*, 1954, **45**, No. 367, 823–843, doi:10.1080/14786440808520496.
14. Xing M.-J., Li B.-H., Yu Z.-T., Chen Q., *Commun. Theor. Phys.*, 2015, **64**, No. 2, 237–243, doi:10.1088/0253-6102/64/2/237.
15. Yang R., Zhu C., Wei Q., Zhang D., *Solid State Commun.*, 2017, **267**, 23–28, doi:10.1016/j.ssc.2017.09.008.
16. Yang R., Zhu C., Wei Q., Du Z., *J. Phys. Chem. Solids*, 2017, **104**, 68–78, doi:10.1016/j.jpcs.2016.12.032.
17. Jiao Z.-Y., Ma S.-H., Yang J.-F., *Solid State Sci.*, 2011, **13**, No. 2, 331–336, doi:10.1016/j.solidstatesciences.2010.11.030.
18. Feng J., Xiao B., Chen J.C., Zhou C.T., *Solid State Sci.*, 2009, **11**, No. 1, 259–264, doi:10.1016/j.solidstatesciences.2008.04.015.
19. Fan Q., Wei Q., Yan H., Zhang M., Zhang Z., Zhang J., Zhang D., *Comput. Mater. Sci.*, 2014, **85**, No. 4, 80–87, doi:10.1016/j.commatsci.2013.12.045.
20. Tosi M.P., Fumi F.G., *Phys. Rev.*, 1963, **131**, No. 4, 1458–1465, doi:10.1103/PhysRev.131.1458.

Структурні, механічні, електронні, оптичні і термодинамічні властивості $t\text{-X}_3\text{As}_4$ ($X = \text{Si}, \text{Ge}$ і Sn) з першопринципних розрахунків

Р. Янг¹, Ю. Ма¹, К. Вей¹, Д. Жанг², І. Жоу³

¹ Школа фізики та оптоелектронної інженерії, громадський університет у Сіані, 710071, Китай

² Національний суперкомп'ютерний центр в Шеньчжені, Шеньчжень 518055, Китай

³ Інститут електроніки та технологічних досліджень Лейхуа, Авіаційна промислова корпорація Китаю, Усі, Цзянсу 214063, Китай

Структурні, механічні, електронні, оптичні і термодинамічні властивості $t\text{-X}_3\text{As}_4$ ($X = \text{Si}, \text{Ge}$ і Sn) з тетрагональною структурою досліджено з першопринципних розрахунків. Результати обчислень показують, що ці сполуки є механічно і динамічно стійкими. Дослідивши пружну анізотропію, встановлено, що анізотропія $t\text{-Sn}_3\text{As}_4$ є сильніша, ніж анізотропія $t\text{-Si}_3\text{As}_4$ і $t\text{-Ge}_3\text{As}_4$. Зонна структура і густина станів показують, що $t\text{-X}_3\text{As}_4$ (Si, Ge і Sn) — це напівпровідники з вузькими забороненими зонами. На основі аналізу різниці електронної густини встановлено, що у $t\text{-X}_3\text{As}_4$ атоми As отримують електрони, а X атоми втрачають електрони. Розраховані статичні діелектричні сталі, $\epsilon_1(0)$, є 15.5, 20.0 і 15.1 еВ відповідно для $t\text{-X}_3\text{As}_4$ ($X = \text{Si}, \text{Ge}$ і Sn). Границя Дюлонга-Пті $t\text{-X}_3\text{As}_4$ є біля $10 \text{ Дж} \cdot \text{моль}^{-1} \cdot \text{К}^{-1}$. Термодинамічна стійкість поступово знижується від $t\text{-Si}_3\text{As}_4$ до $t\text{-Ge}_3\text{As}_4$ і до $t\text{-Sn}_3\text{As}_4$.

Ключові слова: $t\text{-X}_3\text{As}_4$, механічні властивості, оптоелектронні властивості, термодинамічні властивості, першопринципні розрахунки